JACS
JOURNAL OF THE AMERICAN CHEMICAL SOCIETY
pubs.acs.org/JACS
Article

Artificial Frustrated Lewis Pairs for Ampere-Level Ammonia Synthesis and High-Power-Density Zinc-Nitrate Battery

Shaoce Zhang,[#] Dong Chen,[#] Rong Zhang, Xinru Yang, Xintao Ma, Chuan Li, Huilin Cui, Zhiquan Wei, Yiqiao Wang, Peng Chen, Xun Guo, Shixun Wang, Johnny C. Ho, Ying Guo,* and Chunyi Zhi*

Cite This: J. Am. Chem. Soc. 2025, 147, 41433−41442

Read Online

ACCESS | Metrics & More | Article Recommendations | Supporting Information

ABSTRACT: Cu-based electrocatalysts exhibit superior reduction kinetics in the electrochemical nitrate reduction reaction (NO_3RR) and suppress competing hydrogen evolution reaction, making NO_3RR an alternative to the traditional Haber−Bosch process in NH_3 production. However, the NO_3RR in NH_3 production involves a nine-proton and eight-electron process, and its performance is constrained by the poor capacity to generate protons. In this study, frustrated Lewis pairs (FLPs) were introduced into Cu-based catalysts to create La-doped Cu_2O, in which the FLPs [Cu−O−La−O_v] (where v denotes vacancy) formed by the Lewis acidic sites O_v and Lewis basic sites O in the Cu−O−La motif served as active sites. These active sites facilitated H_2O dissociation, providing ample protons for the NO_3RR hydrogenation. The La_9−CuO_x catalyst exhibited an ultralow NH_3 production overpotential of only 290 mV, achieving an NH_3 current density of 1.76 A cm^{-2} at −0.4 V vs the reversible hydrogen electrode, with an NH_3 yield rate of 139.5 mg h^{-1} cm^{-2} and Faradaic efficiency of 98.9%. Due to the superior NO_3RR performance of La_9−CuO_x, a La_9−CuO_x-based Zn-NO_3^- battery achieved a remarkable power density of 80.6 mW cm^{-2}, with an NH_3 yield rate of 21.4 mg h^{-1} cm^{-2}. This study clarifies the role of FLPs in facilitating the NO_3RR and achieves an efficient Zn-NO_3^- battery to accomplish electricity generation and NH_3 production simultaneously.

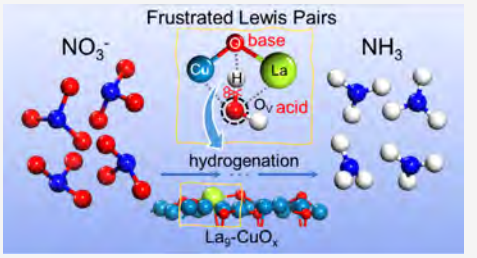

1. INTRODUCTION

Ammonia (NH_3) is a fundamental component in the production of fertilizers, pharmaceuticals, and nitrogen-based industrial chemicals.[1−3] As a hydrogen carrier, NH_3 has high energy density and is thus an exceptional candidate for energy storage and transportation.[4] Given the challenges associated with NH_3 production through the traditional Haber−Bosch process, including substantial energy consumption, carbon emissions, and reliance on fossil fuels, increasing focus has been devoted to the development of sustainable methods for NH_3 synthesis.[5−7] Recently, the aqueous electrochemical nitrate reduction reaction (NO_3RR) has gained attention as a potential alternative to the Haber−Bosch route.[8,9] NO_3^- ions are abundant in the environment, especially in wastewater.[10,11] Additionally, the incomplete conversion of NO_3^- into NO_2^- poses carcinogenic and other health risks.[12] Thus, the use of aqueous NO_3RR for NH_3 production offers a compelling solution for treating wastewater containing NO_3^-, thus turning a harmful substance into a valuable resource.

The use of NO_3RR in NH_3 production involves a complex nine-proton and eight-electron transfer process that entails notable challenges, including slow kinetics, the potential generation of byproducts, and a competing hydrogen reduction reaction (HER).[13−15] Therefore, developing catalysts with high activity and selectivity is crucial. Cu-based catalysts suppress HER activity due to their unfavorable hydrogen adsorption and exhibit a *d* orbital energy level similar to the LUMO π^* of NO_3^-, indicating promise for application in NO_3RR.[16] Nevertheless, the inferior proton generation ability of Cu-based catalysts hinders their performance during the hydrogenation process of NO_3RR.[17,18] The proton source for the aqueous NO_3RR is H_2O molecules, whose activation and dissociation can be leveraged to ensure efficient NO_3^--to-NH_3 conversion with Cu-based catalysts.

Frustrated Lewis pairs (FLPs), a promising surface modification strategy in catalysis, can maintain the interaction between Lewis acids and bases by steric hindrance, thereby activating reactant molecules under ambient conditions.[19,20] FLPs can cleave H−H bonds through unsaturated sites to achieve efficient H_2 activation and dissociation.[21] They can also adsorb CO_2 through interactions between the two O atoms of CO_2 and two Lewis acidic sites, forming a covalent bond between the C atom and Lewis basic sites. This process elongates the C═O bond and decreases the O−C−O angle, enhancing CO_2 activation.[22] Accordingly, we hypothesize that

Received: June 30, 2025
Revised: October 18, 2025
Accepted: October 21, 2025
Published: October 29, 2025

https://doi.org/10.1021/jacs.5c11084
J. Am. Chem. Soc. 2025, 147, 41433−41442

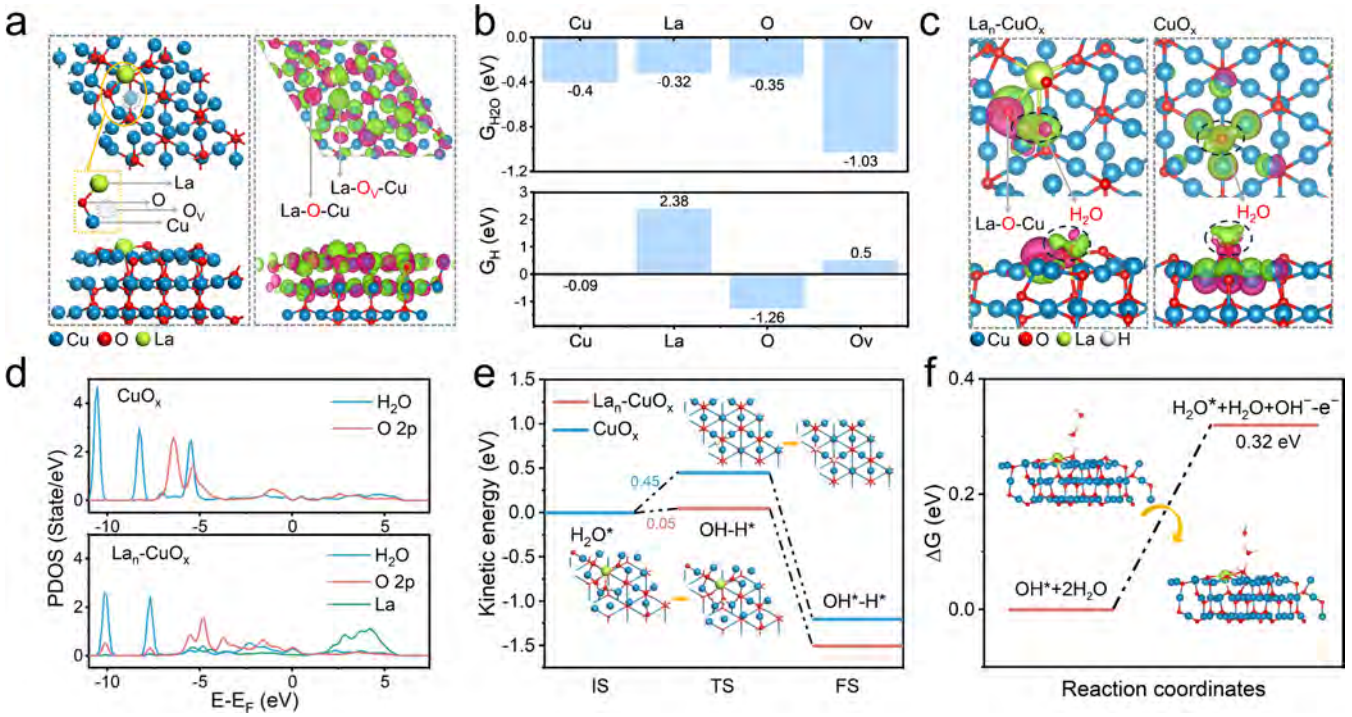

Figure 1. DFT calculations. a) Top and side views of the optimized atomic structure and differential charge density of La_n-CuO_x obtained by comparing the electron density between Cu_2O and La_n-CuO_x. The inset shows a motif of FLP. b) Gibbs free energy of adsorbed H_2O^* and H* at various sites in La_n-CuO_x. c) Differential charge density of La_n-CuO_x and CuO_x with H_2O adsorption. d) Projected density of states of H_2O adsorbed on CuO_x and La_n-CuO_x. e) Kinetic H_2O dissociation barrier on La_n-CuO_x and CuO_x; IS denotes the initial state, TS denotes the transition state, and FS denotes the final state. f) Energy barrier for refreshing Lewis acid sites.

H_2O molecules can be activated by the design of suitable FLPs. The negatively charged O and positively charged H of the H_2O molecule could be adsorbed on Lewis acidic/basic sites, thereby generating protons on Cu-based catalysts for hydrogenation during NO_3RR.

In this study, we introduced FLPs into Cu-based catalysts for the NO_3RR by doping rare-earth La single atoms into Cu_2O, creating a La_n-CuO_x (*n* represents the doping amount of La) catalyst. The introduction of La atoms, which possess high electrophilicity and an ionic radius significantly larger than that of Cu^+, induces pronounced lattice distortion in the Cu_2O structure, thereby promoting the formation of abundant oxygen vacancies (O_vs). The consequent formation of Lewis acidic site O_v and Lewis basic site O in the La−O−Cu motif led to the creation of [Cu−O−La−O_v] FLPs, which activated H_2O molecules to generate protons, realizing efficient hydrogenation in the NO_3RR. This mechanism enhanced the NO_3RR performance of the fabricated La_9-CuO_x catalyst, which surpassed the performance of nearly all previously reported catalysts during the NO_3RR for NH_3 production. Additionally, we assembled a high-performance Zn-NO_3^- battery using La_9-CuO_x as the cathode, which simultaneously generated electricity and enabled NO_3^--to-NH_3 conversion.

2. RESULTS AND DISCUSSION

2.1. Theoretical Investigation. Density functional theory (DFT) calculations were performed on a model of the La_n-CuO_x catalyst to investigate the role of the FLPs. Figure 1a displays the atomic structure and differential charge density of La_n-CuO_x. Because La has a larger ionic radius than Cu, La doping introduces O_vs in Cu_2O.[23,24] In our model, we constructed an O_v to illustrate the effects of La doping. The differential charge density revealed that the O_v region was the charge depletion region, and the O atom in La−O−Cu was the charge accumulation region. This finding clearly indicates that the O_v in La−O_v−Cu is an electron receptor (Lewis acid), whereas the O in La−O−Cu is a Lewis base. Due to steric hindrance, these two sites form FLPs.[25] Protons play a key role in hydrogenation during the NO_3RR, and rapid H_2O molecule dissociation ensures sufficient proton provision during the reaction. Lewis acid−base sites can either donate electrons to H_2O molecules or receive electrons from H_2O molecules, thereby facilitating H_2O dissociation to generate protons. Figure 1b illustrates the Gibbs free energies of adsorbed H_2O^* and H* at various sites in La_n-CuO_x. H_2O molecules prefer to be adsorbed at the O_v sites, whereas the O in La−O−Cu has a greater capacity for proton adsorption (Figure S1 and Note S1).

To further investigate the effect of FLPs on H_2O molecule dissociation, we examined the differential charge density of CuO_x and La_n-CuO_x with H_2O adsorption (Figure 1c). For La_n-CuO_x, the O* in H_2O adsorbed onto the Lewis acid site (O_v), whereas the H* in H_2O tended to interact with the Lewis base (the O in La−O−Cu), stretching the molecule between electronically opposite sites and enhancing O−H bond polarization. This phenomenon allows the FLPs to simultaneously stabilize H* (on the Lewis base) and OH* (on the Lewis acid), thereby effectively separating the two species, accelerating proton generation, and ensuring sufficient H* supply for efficient NO_3RR hydrogenation. The projected density of states (Figure 1d) further confirmed the strength of this interaction, in which a substantial overlap was observed between the 2p orbital in La−O−Cu and the H_2O orbitals. These results indicate that FLPs can substantially enhance

https://doi.org/10.1021/jacs.5c11084
J. Am. Chem. Soc. 2025, 147, 41433−41442

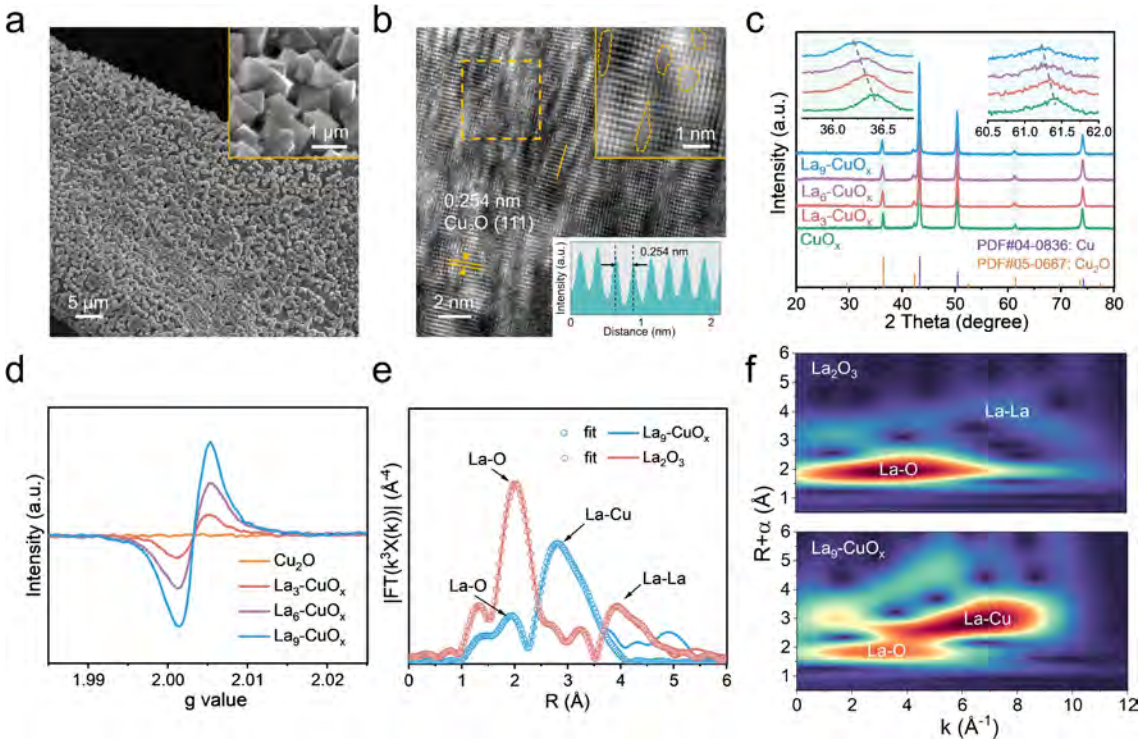

Figure 2. Morphology and structural characterization of catalysts. a) Scanning electron microscopy image of La_9-CuO_x. The inset provides an enlarged view. b) HRTEM image of La_9-CuO_x. The upper inset displays the inverse fast-Fourier transform image of the selected area, and the lower inset displays the corresponding intensity profile along the line. c) XRD patterns of CuO_x, La_3-CuO_x, La_6-CuO_x, and La_9-CuO_x. The insets display XRD results in an enlarged range. d) EPR spectroscopy results. e) Fourier-transformed EXAFS spectra in R space. f) Wavelet transform EXAFS spectra of La_2O_3 and La_9-CuO_x.

H_2O dissociation to generate protons. The H_2O dissociation barrier calculated for La_n-CuO_x was only 0.05 eV (Figure 1e), much lower than that in CuO_x (0.45 eV), suggesting that the Lewis acid O_v site and basic O site in La−O−Cu formed after La doping were highly effective for H_2O dissociation. The H* generated during H_2O dissociation preferentially adsorbs onto the O site in La−O−Cu ($O_v-H_2O^*$ + La−O → O_v−OH* + La−O−H*), while the OH* shifts to the O_v site. According to the water-assisted proton exchange pathway,[25,26] the OH* retained at the Lewis acid site (O_v) undergoes proton exchange with interfacial water molecules. This process ultimately leads to the release of OH^- into the electrolyte and the regeneration of H_2O molecules at the O_v, thereby enabling a continuous water splitting process. the calculated energy barrier for refreshing Lewis acid sites ($O_v-OH^* + H_2O$ (aq) → $O_v-H_2O^* + OH^-$ (aq)) is 0.32 eV (Figure 1f), which is lower than that of CuO_x (Figure S2). This result highlights the promoting role of FLPs in facilitating the hydrogenation process of the NO_3RR.

2.2. Synthesis of La_n-CuO_x Electrocatalyst. We synthesized La_n-CuO_x catalysts with different La contents: La_3-CuO_x (La content 2.7 wt %), La_6-CuO_x (6.2 wt %), and La_9-CuO_x (9.4 wt %), as measured using inductively coupled plasma optical emission spectroscopy. As illustrated in the scanning electron microscopy image in Figure 2a, the as-prepared La_9-CuO_x catalyst exhibited an octahedral morphology on the Cu foam substrate with a uniform particle size. Cu_2O and CuO_x (vacuum-annealed Cu_2O) were also fabricated as counterparts (Figure S3). High-resolution transmission electron microscopy (HRTEM) of La_9-CuO_x in Figure 2b demonstrated a lattice spacing of 0.254 nm belonging to Cu_2O (111), which was 3.25% larger than that of pure Cu_2O and CuO_x (0.246 nm; Figure S3b,d) due to La doping. Notably, the inverse fast-Fourier-transform image of La_9-CuO_x revealed lattice defects (inset in Figure 2b) aligned with those of CuO_x (inset in Figure S3d), which are attributable to the O_vs induced by the difference in ionic radii between La and Cu during the doping process.[27−29] As shown in the scanning TEM and energy-dispersive spectroscopy mapping images (Figure S4), the distribution of Cu, La, and O elements of the La_9-CuO_x catalyst indicates the homogeneous doping of La. The X-ray diffraction patterns in Figure 2c and S5 exhibit the (111), (200), and (220) characteristic peaks that correspond to Cu_2O (JCPDS 05-0667). The doping of La did not result in any new distinctive peaks in the samples. As La doping increased, peak shifts toward angles lower than those of pure Cu_2O and CuO_x indicate lattice expansion, consistent with the HRTEM results. However, excessive La doping induces severe lattice defects and significantly reduces crystallinity, which may decrease the catalytic performance (Figure S6 and Note S2).

During X-ray photoelectron spectroscopy (XPS) testing, Ar^+-cluster etching was used to eliminate the effect of air oxidation on the catalyst surface. Figure S7a displays high-resolution La 3d XPS for La $3d_{5/2}$, indicating the oxidation state of La in La_9-CuO_x. Additionally, the high-resolution XPS of Cu 2p (Figure S7b) and Cu LMM Auger spectra (Figure S7c) revealed the presence of Cu^0 from the Cu foam substrate and Cu^+ species in La_9-CuO_x. The XPS spectra of the O 1s were deconvoluted into three peaks at 529.9, 531.3, and 533.2 eV (Figure S7d), which were assigned to lattice oxygen (O_l), O_v, and chemical-absorbed oxygen (O_c), respectively.[30,31]

https://doi.org/10.1021/jacs.5c11084
J. Am. Chem. Soc. 2025, 147, 41433−41442

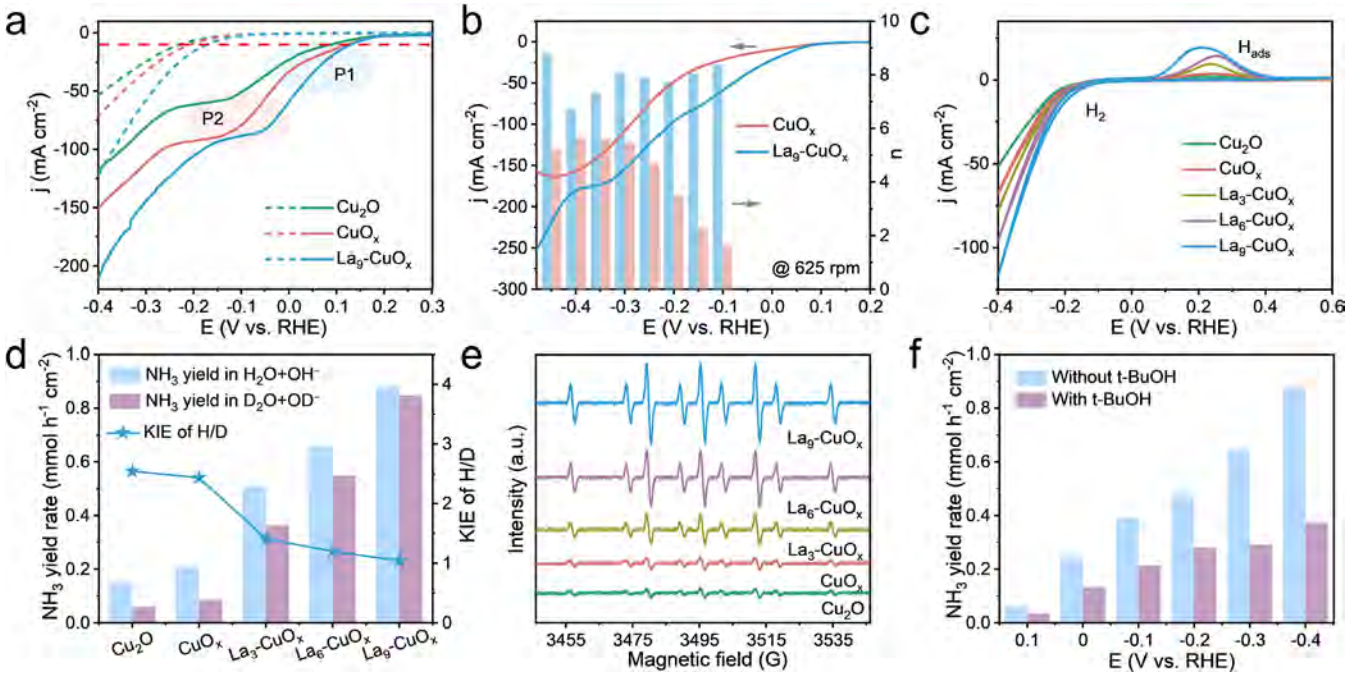

Figure 3. Generation of NH_3 during NO_3RR through an active H_{ads} supply. a) LSV curves (80% *iR* corrected) of Cu_2O, CuO_x, and La_9-CuO_x with (solid lines) and without (dashed lines) 0.1 M NO_3^- in 1 M KOH at a scan rate of 1 mV s^{-1}. The position of the horizontal red dashed line is 10 mA cm^{-2}. P1 and P2 areas represent current peak regions. b) LSV curves (80% *iR* corrected) at 625 rpm and electron transfer numbers for CuO_x and La_9-CuO_x on a rotating disk electrode in an electrolyte containing 0.1 M KNO_3 and 1 M KOH at a scan rate of 10 mV s^{-1}. c) CV curves of Cu_2O, CuO_x, La_3-CuO_x, La_6-CuO_x, and La_9-CuO_x without NO_3^- at a scan rate of 2 mV s^{-1}. d) NH_3 yield rate of catalysts in various electrolytes at −0.4 V vs RHE and corresponding KIE of H/D. e) EPR results of DMPO-H after a 10-min chronoamperometry test of various catalysts in an electrolyte containing 1 M KOH. f) NH_3 yield rate of La_9-CuO_x with and without 0.5 M *t*-BuOH.

La_9-CuO_x had the highest $O_v/(O_l + O_v + O_c)$ ratio (Figure S7e) among the samples, consistent with the electron paramagnetic resonance (EPR) spectroscopy results indicating that most O_vs were present in La_9-CuO_x (Figure 2d). The XPS and EPR results revealed a positive correlation between the O_v concentration and La doping content, confirming that the O_v in La_n-CuO_x originated from La doping, which induced abundant FLP sites. X-ray absorption near-edge structure spectroscopy and extended X-ray absorption fine structure (EXAFS) spectroscopy were then performed to investigate the valence state and local coordination environment of La in La_9-CuO_x. La L_3-edge adsorption (Figure S8) indicated the positive charge state of La in La_9-CuO_x. In the Fourier-transformed EXAFS in the R space of La_9-CuO_x (Figure 2e), the peak at approximately 1.9 Å was ascribed to the La−O coordination structure, whereas no La−La scattering path signal was observed, confirming the atomic dispersion of La in the catalyst. The quantitative results from the EXAFS analysis of La_9-CuO_x (Figures 2e, S8, S9 and Table S1) revealed coordination numbers of 4.4 and 6.5 for La−O and La−Cu, respectively, with average La−O and La−Cu bond lengths of 2.43 and 3.34 Å, respectively. These results were similar to those of our DFT calculations. The La−La coordination signal was absent in the wavelet transform EXAFS results (Figure 2f), further supporting the atomic distribution of La in La_9-CuO_x.

2.3. FLP-Promoted NO_3RR. Linear sweep voltammetry (LSV) curves at a scan rate of 1 mV s^{-1} revealed that the current of Cu_2O, CuO_x, and La_9-CuO_x considerably increased with the addition of NO_3^- (Figure 3a), indicating notable NO_3RR activity. The overpotential at 10 mA cm^{-2} (η_{10}) in the kinetic control process is a crucial parameter for the evaluation of catalytic activity, representing the difference between the potential at a current of 10 mA cm^{-2} and the E_0 (690 mV) in the NO_3RR. O_vs lowered the η_{10} from 603 mV in Cu_2O to 566 mV in CuO_x and 559 mV in La_9-CuO_x, indicating a reduced NO_3RR energy barrier. The LSV curves in Figure 3a display two current inflection points corresponding to the reduction of NO_3^- to NO_2^- through two-electron transfer (P1 area) and a subsequent reduction of NO_2^- to NH_3 through six-electron transfer (P2 area).[32,33] The Tafel plots in the P1 area displayed slightly lower slopes for CuO_x and La_9-CuO_x than Cu_2O (Figure S10), suggesting that O_v promoted the reduction of NO_3^- to NO_2^-.[34] In the P2 area, the LSV curve of La_9-CuO_x exhibited a notable positive shift of approximately 60 mV, indicating that FLPs considerably reduced the reaction barrier and promoted kinetics in the reduction of NO_2^- to NH_3. After normalizing to the electrochemically active surface area (ECSA), La_9-CuO_x maintained the highest current density compared to the counterparts, confirming the superior intrinsic activity of La_9-CuO_x (Figures S11, S12 and Note S3). Koutecký−Levich (K−L) plots were created to identify the electron transfer number (n) in the NO_3RR (Figures 3b and S13). CuO_x exhibited two-electron transfer at −0.1 V, indicating NO_3^--to-NO_2^- conversion, and subsequent six-electron transfer at −0.3 V, indicating NO_2^--to-NH_3 conversion. La_9-CuO_x exhibited eight-electron transfer within the potential range, confirming an unobstructed reduction process compared with that of CuO_x. These findings suggest the benefits of FLPs for promoting the NO_2^--to-NH_3 conversion.

In the cyclic voltammogram (CV) test, the peak area at approximately 0.3 V vs RHE was positively correlated with the hydrogen adsorption (H_{ads}) enrichment of the electrode

https://doi.org/10.1021/jacs.5c11084
J. Am. Chem. Soc. 2025, 147, 41433−41442

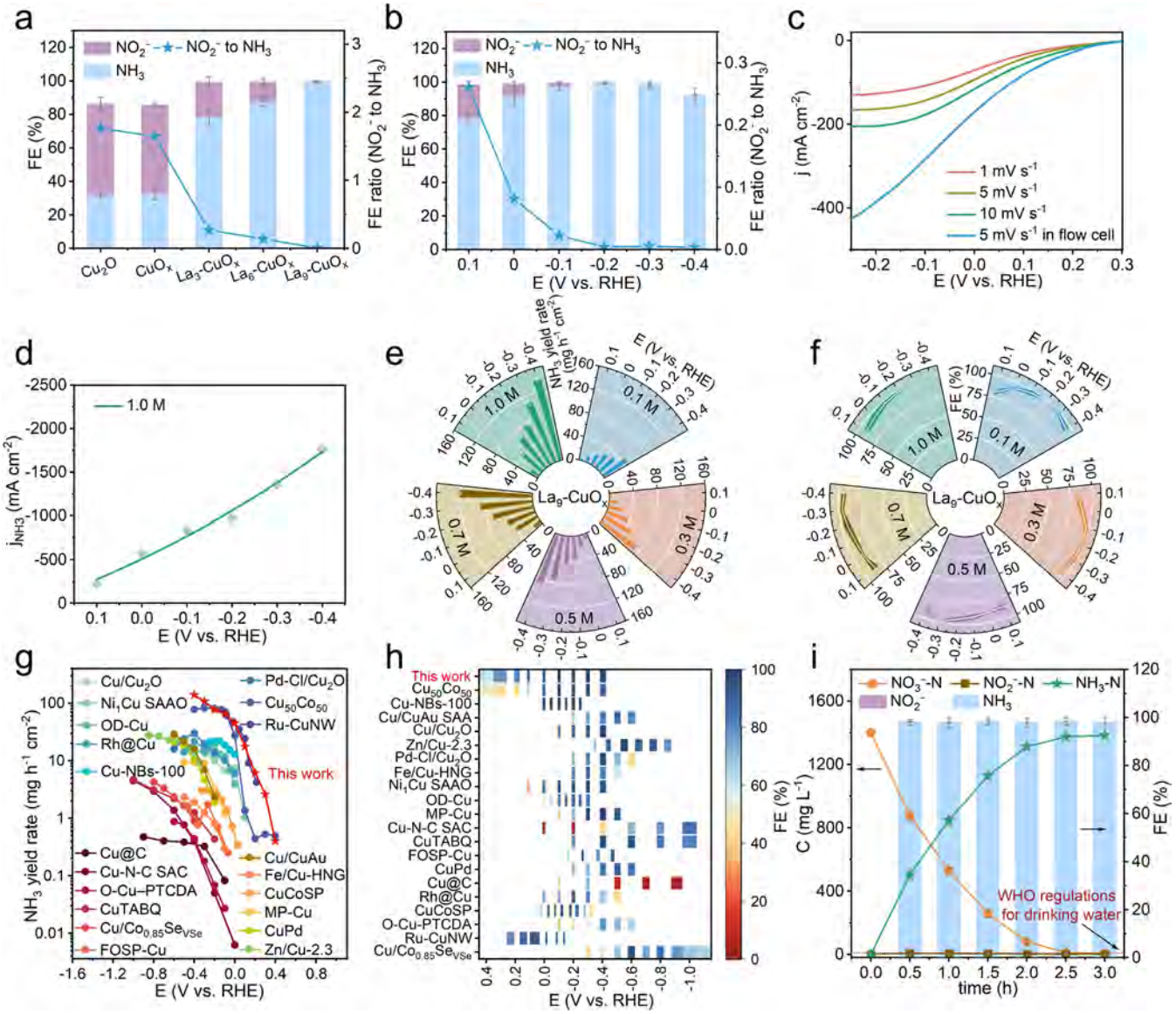

Figure 4. Electrochemical performance of the catalysts. a) FE and corresponding FE ratio of NO_2^- and NH_3 for various catalysts at −0.2 V vs RHE. b) FE and corresponding FE ratio of NO_2^- and NH_3 for La_9-CuO_x at different potentials. c) LSV curves of La_9-CuO_x at various scan rates in the H-type cell and at a scan rate of 5 mV s^{-1} in the flow cell (blue line). The electrolyte in both cells contained 1 M KOH and 0.1 M KNO_3. d) NH_3 partial current densities of La_9-CuO_x in an electrolyte containing 1 M KOH and 1 M KNO_3 at a potential range of 0.1 V to −0.4 V vs RHE. e) NH_3 yield rate and f) FE of La_9-CuO_x in an electrolyte containing 1 M KOH and KNO_3 with various concentrations. g,h) Comparison of g) NH_3 yield rate and h) FE of La_9-CuO_x with the performance of previously reported catalysts in NO_3RR for NH_3 generation. (i) Test of NO_3^- removal at −0.4 V vs RHE using La_9-CuO_x in an electrolyte containing 1 M KOH and 0.1 M KNO_3. Abbreviations in g and h are defined as follows: HNG, holey edge sites of nitrogen-doped graphene; SAAO, single-atom alloy oxide; OD, oxide-derived; MP, metastable phase; SAC, single-atom catalyst; FOSP, flower-like open-structured polycrystalline; NW, nanowire; SP, PO_4^{3-}-modified sulfides; NB, nanobelt.

surface.[35] As displayed in Figure 3c, the CV curves of an electrolyte containing 1 M KOH had a substantially larger hydrogen peak area in La_n-CuO_x than in CuO_x, which increased with higher La doping amounts. These experimental results suggest that FLPs enhanced the ability of the catalysts to generate H_{ads}. The protonation process during NO_3RR was investigated by examining the kinetic isotope effect (KIE), as expressed by the ratio of the NH_3 yield rate obtained in H_2O and D_2O (Figure 3d).[36] The KIE values of H/D (H_2O/D_2O) for Cu_2O and CuO_x were 2.54 and 2.43, respectively, confirming that sluggish H_2O dissociation limited proton-coupled transfer during the NO_3RR. The KIE value decreased to 1.40 after introducing La and was further reduced to 1.04 when the doping amount increased to 9.4 wt %. This finding indicates that introducing FLPs facilitated H_2O dissociation, thereby enhancing protonation during the NO_3RR. The EPR curves (Figure 3e) were measured by using the spin trap agent 5,5-dimethyl-1-pyrroline-*N*-oxide (DMPO). Nine peaks with an intensity ratio of 1:2 confirmed the presence of DMPO-H.[37] The peak intensity in the electrolyte without NO_3^- notably increased after the introduction of FLPs and exhibited a positive correlation with the La doping amounts. The intensity of the DMPO-H peak sharply decreased with the addition of NO_3^- to the electrolyte and continued to decline as the NO_3^- concentration increased (Figure S14). These observations suggest that FLPs enhanced H_2O dissociation to produce H_{ads}

https://doi.org/10.1021/jacs.5c11084
J. Am. Chem. Soc. 2025, 147, 41433−41442

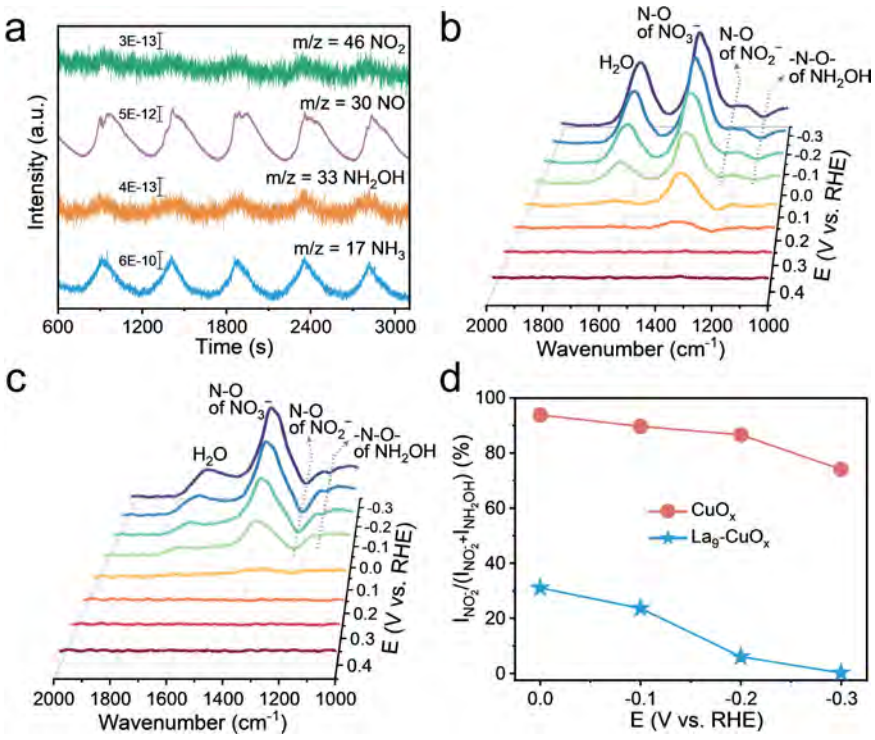

Figure 5. In situ analyses during electrochemical measurements. a) Online differential electrochemical mass spectrometry of La_9-CuO_x in the NO_3RR. b,c) In situ ATR-FTIR of b) La_9-CuO_x and c) CuO_x at various potentials. d) Ratio of NO_2^- peak intensity to total peak intensity of the intermediates generated by CuO_x and La_9-CuO_x $\left(\frac{I_{NO_2^-}}{I_{NO_2^-}+I_{NH_2OH}}\right)$ at different potentials.

for protonation during the NO_3RR. The addition of the H_{ads}-consuming agent tertiary butanol (*t*-BuOH) considerably decreased the NH_3 yield rate (Figure 3f), highlighting the crucial role of H_{ads} generated by FLPs in the NO_3RR.

2.4. NO_3RR Performance. The catalytic products were quantitatively analyzed using UV−vis spectrophotometry (Figures S15−S17). Hydrazine was not detected in any catalyst. As depicted in Figure 4a, the Faradaic efficiency (FE) of NO_2^- and NH_3 for CuO_x at the applied potential of −0.2 V vs RHE was 53.3% and 32.4%, respectively. This finding indicates that a substantial amount of NO_2^- accumulated on the catalytic surface due to sluggish hydrogenation during the NO_3RR. The introduction of FLPs considerably reduced the NO_2^-/NH_3 FE ratio from 1.64 to 0.27, and this ratio further decreased to nearly zero as La doping increased, demonstrating enhanced protonation of NO_2^- conversion to NH_3. Meanwhile, electrochemical impedance spectroscopy, as shown in Figure S18, reveals that increasing La content reduces charge-transfer resistance, enhancing electron transport during NO_3RR. Even at a low overpotential (η = 590 mV), La_9-CuO_x exhibited a low FE ratio of 0.26 (Figure 4b), indicating the strength of this catalyst in facilitating efficient NO_2^--to-NH_3 conversion. At potentials greater than −0.1 V vs RHE, NO_3^- was almost completely converted to NH_3.

The as-prepared La_9-CuO_x exhibited a remarkable ability to generate NH_3 in the NO_3RR. However, this catalyst was also affected by diffusion control during the reaction (Figure 4c). To eliminate this effect, a homemade flow cell was used in electrocatalysis, and electrolyte replenishment during the experiment ensured a stable NO_3^- concentration. The current density for NH_3 production of La_9-CuO_x increased along with the potential and NO_3^- concentration, reaching a peak of 1.76 A cm^{-2} (Figures 4d and S19). At −0.4 V vs RHE in an electrolyte containing 1 M KOH and 1 M KNO_3, NH_3 was produced with an FE of 98.9% (Figure 4e) and a yield rate of 139.5 mg h^{-1} cm^{-2} (Figure 4f). These performances outperformed nearly all previously reported catalysts in the NO_3RR for NH_3 generation, demonstrating its potential to meet high industrial demands (Figure 4g,h and Table S2). The FE for NH_3 production of catalysts with varying La contents was further evaluated by using a flow cell (Figure S20). Consistent with the H-cell result tendency shown in Figure 4a, the FE increased with higher La content, further confirming the critical role of FLPs in promoting the selectivity of NO_3^- reduction. Moreover, La_9-CuO_x exhibited a maximum energy efficiency of 43.6% at 0.1 V vs RHE in an electrolyte comprising 1 M KOH and 1 M KNO_3 (Figure S21). At an η of only 290 mV, the NH_3 yield rate and FE were 0.4 mg h^{-1} cm^{-2} and 62.2%, respectively (Figure S22). This η was considerably lower than those of most of the catalysts reported in the literature (Figure S23 and Table S2).

To identify the source of the N in the NH_3 produced during NO_3RR, electrolysis with La_9-CuO_x was conducted under two conditions. One condition involved an open circuit potential with NO_3^- in an electrolyte, and the other involved varied potentials without NO_3^- as a feedstock. Negligible NH_3 was detected under both conditions (Figure S24). Moreover, $^{15}NO_3^-$ was employed instead of $^{14}NO_3^-$ for the NO_3RR to conduct ^1H nuclear magnetic resonance (NMR) (Figure S25), and only the doublet coupling characteristic peak for $^{15}NH_4^+$ was observed (Figure S25a).[38,39] The results obtained by quantitative NMR were consistent with those obtained by UV−vis (Figure S25d). These results confirmed that NH_3 originated from the NO_3RR. A stability test of La_9-CuO_x using a flow cell at the applied potential of −0.4 V vs RHE

https://doi.org/10.1021/jacs.5c11084
J. Am. Chem. Soc. 2025, 147, 41433−41442

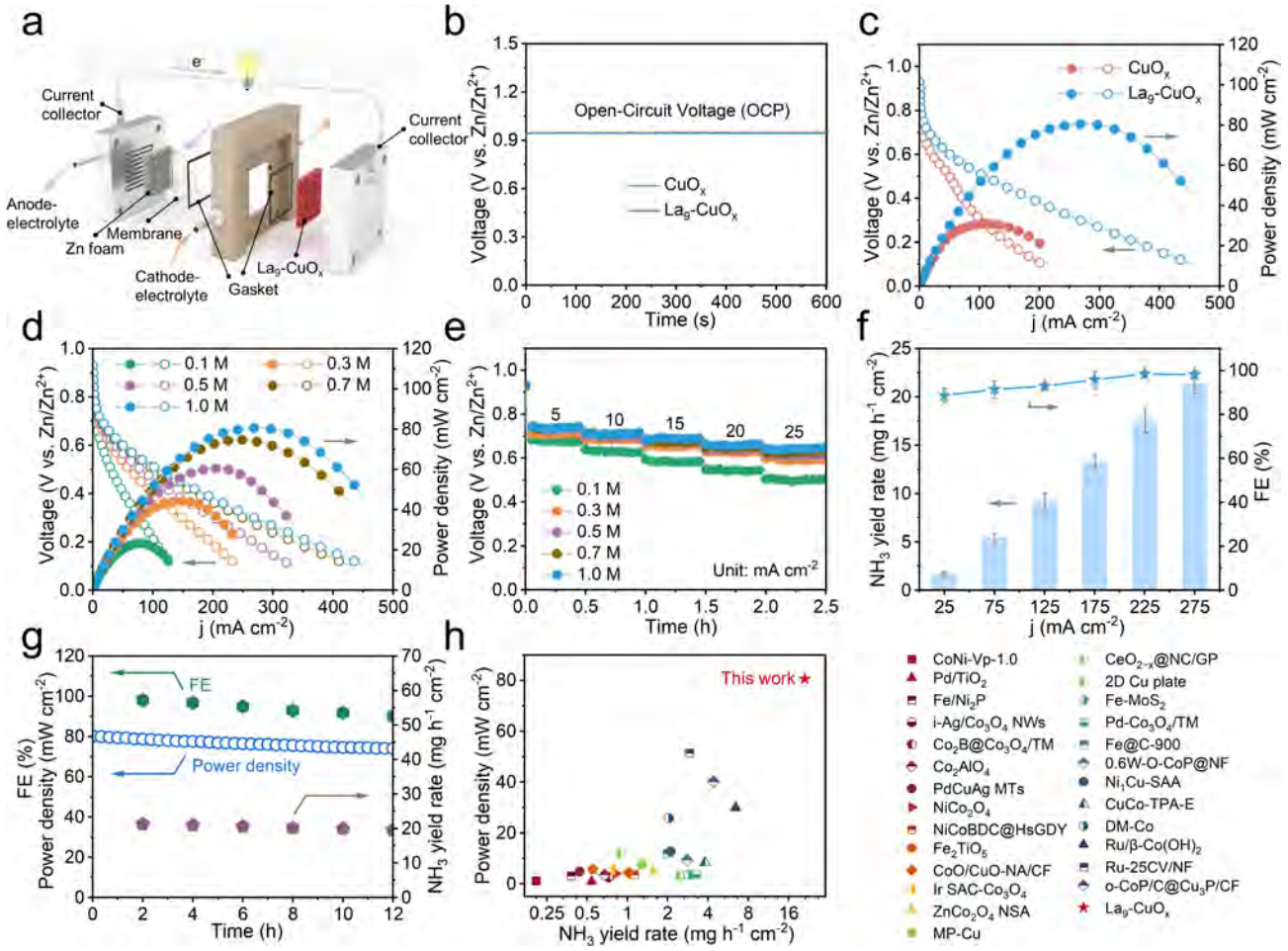

Figure 6. Electrochemical performance of the Zn-NO_3^- battery. a) Diagram of Zn-NO_3^- battery. b) Open circuit potential curves, and c) discharge polarization plots and power densities of CuO_x- and La_9−CuO_x-based Zn-NO_3^- batteries obtained with 1 M NO_3^-. d) Discharge polarization plots and power densities and e) discharging tests of La_9−CuO_x-based Zn-NO_3^- battery in 1 M KOH at various current densities and NO_3^- concentrations. f) NH_3 yield rate and FE of La_9−CuO_x-based Zn-NO_3^- battery. g) Stability tests of La_9−CuO_x-based Zn-NO_3^- battery at 275 mA cm^{-2} in 1 M KOH and 1 M NO_3^-. h) Power density and NH_3 yield rate of La_9−CuO_x-based Zn-NO_3^- battery compared with those of Zn-NO_3^- batteries developed in previous studies. Abbreviations in h) are defined as follows: Vp, phosphide; NWs, nanowires; TM, Ti mesh; MTs, mesoporous nanotubes; BDC, benzenedicarboxylic acid; NA, nanoarray; CF, Cu foam; SAC, single-atom catalyst; NSA, nanosheet array; MP, metastable phase; NC, N-doped carbon; GP, graphite paper; NF, nickel foam; SAA, single-atom alloy; TPA, terephthalic acid; DM, dense membrane.

revealed a negligible decline in the NH_3 yield rate and FE over 10 cycles (Figure S26). Following the stability test, the morphology and crystalline structure investigation revealed no notable changes (Figure S27), suggesting the remarkable stability of La_9−CuO_x, which can be attributed to La-doping-induced electronic structure modulation. Furthermore, inductively coupled plasma mass spectrometry (ICP-MS) analysis of the electrolyte after the long-term cycling stability test (Table S3) revealed negligible La leaching, confirming that La atoms remained stably anchored in the catalyst lattice without significant dissolution.

Based on the superior NO_3RR performance of La_9−CuO_x, its application in NO_3^- removal from wastewater appears particularly promising. The World Health Organization (WHO) stipulates that NO_3^- and NO_2^- content in drinking water should remain below 11.3 and 0.91 mg L^{-1}. However, conventional wastewater treatment technologies, including biological methods and ion exchange techniques, exhibit limitations such as the generation of pathogenic bacteria and secondary pollution risks.[10] Therefore, the catalytic approach demonstrates exceptional potential for efficiently removing aqueous nitrogen species, offering solutions for achieving regulatory-compliant wastewater treatment and enabling resource recovery. We evaluate the performance of La_9−CuO_x for NO_3^- removal, in which the NO_3^- concentration was quantitatively analyzed by using UV−vis spectrophotometry (Figure S28). Notably, a 99.2% NO_3^- removal rate was achieved in an electrolyte with 0.1 M NO_3^- at −0.4 V vs RHE over 2.5 h, with a corresponding NH_3 FE of 98.4% and negligible production of NO_2^- (Figure 4i). The remaining NO_3^- concentration was much lower than the threshold for drinking water established by the WHO.[36] The obtained electrolyte was then subjected to Ar stripping for product collection, effectively removing 96.3% of dissolved NH_3 due to its high vapor pressure (Figure S29). The evolved NH_3 was absorbed in a H_2SO_4 solution with 93.3% capture efficiency, followed by rotary evaporation to obtain 89.2% $(NH_4)_2SO_4$ powder. These findings suggest the superior capability of La_9−CuO_x in practical applications.

https://doi.org/10.1021/jacs.5c11084
J. Am. Chem. Soc. 2025, 147, 41433−41442

2.5. Mechanistic Insight by In Situ Analysis. Online differential electrochemical mass spectrometry and in situ attenuated total reflection Fourier transform infrared spectroscopy (ATR-FTIR) were performed to elucidate the intermediate products of La_9-CuO_x during NO_3RR. As illustrated in Figure 5a, NH_3, NO, NH_2OH, and NO_2 exhibited mass-to-charge (m/z) signals of 17, 30, 33, and 46, respectively.[40] Similar features between the peaks across five cycles indicated a stable NO_3^- reduction. In Figure 5b and c, the upward band in the ATR-FTIR spectra located at 1390 cm^{-1} and the concurrent downward band at 1246 cm^{-1} correspond to the consumption of NO_3^- and production of NO_2^-. The peaks of La_9-CuO_x appeared at a more positive potential than those of CuO_x (Figure 5c). The upward band at 1655 cm^{-1} was assigned to H_2O dissociation for proton generation. The peak of NH_2OH was detected at a potential that was more negative than that of the NO_2^- produced during the reaction. Moreover, shifting to more negative potentials led to a pronounced increase in the NH_2OH peak intensity, accompanied by a concomitant decrease in the NO_2^- peak intensity. These results indicate further hydrogenation during the NO_2^- reduction. The ratio of the NO_2^- peak intensity to the total peak intensity of the intermediates generated by La_9-CuO_x $\left(\frac{I_{NO_2^-}}{I_{NO_2^-}+I_{NH_2OH}}\right)$ suggested a rapid decrease with negative potential shifts. These peak intensity ratios were much lower than those of CuO_x at each applied potential (Figure 5d), indicating that FLPs more effectively facilitated hydrogenation in the NO_3RR. Based on these results, we identified the likely mechanism through which FLPs enhance the NO_3RR. The NO_3RR was hindered by sluggish H_{ads} generation in CuO_x. The FLPs in La_9-CuO_x improved H_2O dissociation, producing an abundance of H_{ads} adsorbed on the Lewis basic site O in La−O−Cu. These H_{ads} facilitated rapid hydrogenation, thereby enhancing the La_9-CuO_x activity during the NO_3RR.

2.6. Aqueous Zn-NO_3^- Battery Performance. The eight-electron transfer process of NO_3^- reduction to NH_3 provides abundant electrons to support battery current output.[41] Considering the ampere-level NH_3 production activity of FLP-promoted NO_3RR and their advantage at low overpotentials, we combined NO_3^- reduction at the cathode and Zn oxidation at the anode to assemble a Zn-NO_3^- battery. The chemical energy of Zn drives electron transfer from the anode to the cathode through the external circuit, achieving simultaneous power generation and the production of high-value-added NH_3 from wastewater.[42,43] As illustrated in Figure 6a, the Zn-NO_3^- battery used 1 M KOH and KNO_3 with various concentrations as the cathode electrolyte and 6 M KOH as the anode electrolyte, separated by a membrane of Nafion 117. Both the Zn-NO_3^- battery using CuO_x as the cathode and that using La_9-CuO_x exhibited an open-circuit voltage of approximately 0.94 V vs Zn^{2+}/Zn (Figure 6b), which was close to the theoretical voltage (1.08 V vs Zn/Zn^{2+}; see calculation details in the Supporting Information). As displayed in the discharging polarization curves (Figure 6c), the power density of the La_9-CuO_x-based Zn-NO_3^- battery reached a maximum of 80.6 mW cm^{-2} at 0.29 V vs Zn^{2+}/Zn due to enhanced reaction kinetics, which was considerably higher than that of the CuO_x-based Zn-NO_3^- battery (30.9 mW cm^{-2} at 0.27 V vs Zn^{2+}/Zn). We also investigated the influence of the NO_3^- concentration on the performance of the La_9-CuO_x-based Zn-NO_3^- battery (Figure 6d). As the NO_3^- concentration increased, the maximum power density rose from 23.2 mW cm^{-2} (at 0.1 M NO_3^-) to 80.6 mW cm^{-2} (at 1 M NO_3^-). The slower rate of increase in power density with respect to the increase in NO_3^- concentration may be due to the inherent kinetic limitations of the NO_3RR. Discharging tests of the La_9-CuO_x-based Zn-NO_3^- battery at different current densities, which used cathodic electrolytes with varying NO_3^- concentrations, revealed a tendency toward a slower decrease in voltage as the NO_3^- concentration increased (Figure 6e). This finding was attributed to the better NO_3RR performance of La_9-CuO_x as the NO_3^- concentration increased from 0.1 to 1 M.

The Zn-NO_3^- battery effectively maintained dual functions of power output and NH_3 production. As displayed in Figure 6f, the La_9-CuO_x-based Zn-NO_3^- battery exhibited a remarkable FE of 98.2% for NH_3 production at an output current density of 275 mA cm^{-2} and an NH_3 yield rate of 21.4 mg h^{-1} cm^{-2}. The FE for NH_3 production remained above 85% across a wide range of current densities, indicating the superior performance of La_9-CuO_x for the NO_3RR. A long-term discharge test of the La_9-CuO_x-based Zn-NO_3^- battery was then conducted at 275 mA cm^{-2} (Figure 6g). Due to the gradual depletion of NO_3^- in the electrolyte over time, the power density decreased slightly. However, the FE of NH_3 remained above 90% throughout this process. The La_9-CuO_x-based Zn-NO_3^- battery exhibited remarkable power output and NH_3 production, surpassing the performance of Zn-NO_3^- batteries reported in previous studies (Figure 6h, Table S4).

3. CONCLUSION

We introduced FLPs into Cu-based catalysts to fabricate La_n-CuO_x, effectively mitigating the poor proton supply in Cu-based catalysts during the hydrogenation process of the NO_3RR. The stable Lewis acidic site O_v and Lewis basic site O within the Cu−O−La motif kept intact by steric hindrance compose FLPs [Cu−O−La−O_v]. These FLPs enhance proton generation through the activation and decomposition of H_2O molecules by pulling apart H* and OH*, ensuring the rapid conversion of NO_2^- to NH_3 and enhancing the efficiency of the NO_3RR for NH_3 synthesis. The La_9-CuO_x catalyst exhibited an ultralow NH_3 production η of 290 mV, with an NH_3 yield rate of 0.4 mg h^{-1} cm^{-2} and FE of 62.2%. Additionally, the current density for NH_3 production reached 1.76 A cm^{-2} at −0.4 V vs RHE, with an NH_3 yield rate of 139.5 mg h^{-1} cm^{-2} and FE of 98.9%. We also developed a Zn-NO_3^- battery that benefited from the superior performance of the La_9-CuO_x cathode. The battery exhibited an impressive power density of 80.6 mW cm^{-2}, with an NH_3 yield rate of 21.4 mg h^{-1} cm^{-2}, achieving simultaneous electricity output and NH_3 production.

■ ASSOCIATED CONTENT

Supporting Information

The Supporting Information is available free of charge at https://pubs.acs.org/doi/10.1021/jacs.5c11084.

Experimental methods and calculation details, catalyst characterizations, electrochemical measurements, additional figures and tables (PDF)

https://doi.org/10.1021/jacs.5c11084
J. Am. Chem. Soc. 2025, 147, 41433−41442

AUTHOR INFORMATION

Corresponding Authors

Ying Guo − *School of Interdisciplinary Studies, Lingnan University, Tuen Mun, New Territories, Hong Kong 999077, China*; Email: yingguo2@ln.edu.hk

Chunyi Zhi − *Department of Materials Science and Engineering, City University of Hong Kong, Kowloon, Hong Kong 999077, China; Materials Innovation Institute for Life Sciences and Energy (MILES), HKU-SIRI, Shenzhen 518048, China; Center for Energy Storage and Department of Mechanical Engineering, The University of Hong Kong, Pokfulam, Hong Kong 999077, China*; orcid.org/0000-0001-6766-5953; Email: cy.zhi@cityu.edu.hk

Authors

Shaoce Zhang − *Department of Materials Science and Engineering, City University of Hong Kong, Kowloon, Hong Kong 999077, China*

Dong Chen − *Department of Materials Science and Engineering, City University of Hong Kong, Kowloon, Hong Kong 999077, China*

Rong Zhang − *Department of Materials Science and Engineering, City University of Hong Kong, Kowloon, Hong Kong 999077, China*

Xinru Yang − *Department of Materials Science and Engineering, City University of Hong Kong, Kowloon, Hong Kong 999077, China*

Xintao Ma − *Department of Materials Science and Engineering, City University of Hong Kong, Kowloon, Hong Kong 999077, China*

Chuan Li − *Department of Materials Science and Engineering, City University of Hong Kong, Kowloon, Hong Kong 999077, China*

Huilin Cui − *Department of Materials Science and Engineering, City University of Hong Kong, Kowloon, Hong Kong 999077, China*

Zhiquan Wei − *Department of Materials Science and Engineering, City University of Hong Kong, Kowloon, Hong Kong 999077, China*

Yiqiao Wang − *Department of Materials Science and Engineering, City University of Hong Kong, Kowloon, Hong Kong 999077, China*

Peng Chen − *Department of Materials Science and Engineering, City University of Hong Kong, Kowloon, Hong Kong 999077, China*

Xun Guo − *Department of Materials Science and Engineering, City University of Hong Kong, Kowloon, Hong Kong 999077, China*

Shixun Wang − *Department of Materials Science and Engineering, City University of Hong Kong, Kowloon, Hong Kong 999077, China*; orcid.org/0000-0002-9165-758X

Johnny C. Ho − *Department of Materials Science and Engineering, City University of Hong Kong, Kowloon, Hong Kong 999077, China*; orcid.org/0000-0003-3000-8794

Complete contact information is available at: https://pubs.acs.org/10.1021/jacs.5c11084

Author Contributions

#S.Z. and D.C. contributed equally to this work.

Notes

The authors declare no competing financial interest.

ACKNOWLEDGMENTS

This work was supported by the Research Grants Council of the Hong Kong Special Administrative Region, China (Project No. T23-713/22-R). We acknowledge the beamline BL11B at the Shanghai Synchrotron Radiation Facility (SSRF), Shanghai Institute of Applied Physics (SINAP), Chinese Academy of Sciences (CAS), for their support in the X-ray absorption spectroscopy analysis.

REFERENCES

(1) Liu, K.; Li, H.; Xie, M.; Wang, P.; Jin, Z.; Liu, Y.; Zhou, M.; Li, P.; Yu, G. Thermally enhanced relay electrocatalysis of nitrate-to-ammonia reduction over single-atom-alloy oxides. *J. Am. Chem. Soc.* **2024**, *146* (11), 7779−7790.

(2) Han, S.; Li, H.; Li, T.; Chen, F.; Yang, R.; Yu, Y.; Zhang, B. Ultralow overpotential nitrate reduction to ammonia via a three-step relay mechanism. *Nat. Catal.* **2023**, *6* (5), 402−414.

(3) Zhang, R.; Li, C.; Cui, H.; Wang, Y.; Zhang, S.; Li, P.; Hou, Y.; Guo, Y.; Liang, G.; Huang, Z. Electrochemical nitrate reduction in acid enables high-efficiency ammonia synthesis and high-voltage pollutes-based fuel cells. *Nat. Commun.* **2023**, *14* (1), 8036.

(4) Liu, S.; Wang, M.; He, Y.; Cheng, Q.; Ji, H.; Huan, Y.; Shen, X.; Zhou, X.; Qian, T.; Yan, C. Molecular Imprinting Technology Enables Proactive Capture of Nitrogen for Boosted Ammonia Synthesis under Ambient Conditions. *Adv. Mater.* **2023**, *35* (51), 2303703.

(5) Liang, J.; Liu, Q.; Alshehri, A. A.; Sun, X. Recent advances in nanostructured heterogeneous catalysts for N-cycle electrocatalysis. *Nano Res. Energy* **2022**, *1* (2), 9120010.

(6) Zhang, X.; Lyu, Y.; Zhou, H.; Zheng, J.; Huang, A.; Ding, J.; Xie, C.; De Marco, R.; Tsud, N.; Kalinovych, V.; et al. Photo-electrochemical N_2-to-NH_3 fixation with high efficiency and rates via optimized Si-based system at positive potential versus $Li^{0/+}$. *Adv. Mater.* **2023**, *35* (21), 2211894.

(7) Li, P.; Li, R.; Liu, Y.; Xie, M.; Jin, Z.; Yu, G. Pulsed nitrate-to-ammonia electroreduction facilitated by tandem catalysis of nitrite intermediates. *J. Am. Chem. Soc.* **2023**, *145* (11), 6471−6479.

(8) Du, H.; Guo, H.; Wang, K.; Du, X.; Beshiwork, B. A.; Sun, S.; Luo, Y.; Liu, Q.; Li, T.; Sun, X. Durable electrocatalytic reduction of nitrate to ammonia over defective pseudobrookite Fe_2TiO_5 nanofibers with abundant oxygen vacancies. *Angew. Chem., Int. Ed.* **2023**, *135* (5), No. e202215782.

(9) Zhao, X.; Jiang, Y.; Wang, M.; Liu, S.; Wang, Z.; Qian, T.; Yan, C. Optimizing intermediate adsorption via heteroatom ensemble effect over RuFe bimetallic alloy for enhanced nitrate electroreduction to ammonia. *Adv. Energy Mater.* **2023**, *13* (31), 2301409.

(10) Wang, Y.; Wang, C.; Li, M.; Yu, Y.; Zhang, B. Nitrate electroreduction: mechanism insight, in situ characterization, performance evaluation, and challenges. *Chem. Soc. Rev.* **2021**, *50* (12), 6720−6733.

(11) Guo, Y.; Zhang, R.; Zhang, S.; Zhao, Y.; Yang, Q.; Huang, Z.; Dong, B.; Zhi, C. Pd doping-weakened intermediate adsorption to promote electrocatalytic nitrate reduction on TiO_2 nanoarrays for ammonia production and energy supply with zinc−nitrate batteries. *Energy Environ. Sci.* **2021**, *14* (7), 3938−3944.

(12) Liang, J.; Li, Z.; Zhang, L.; He, X.; Luo, Y.; Zheng, D.; Wang, Y.; Li, T.; Yan, H.; Ying, B.; et al. Advances in ammonia electrosynthesis from ambient nitrate/nitrite reduction. *Chem* **2023**, *9* (7), 1768−1827.

(13) Chen, D.; Zhang, S.; Yin, D.; Li, W.; Bu, X.; Quan, Q.; Lai, Z.; Wang, W.; Meng, Y.; Liu, C.; et al. Tailored p-orbital delocalization by diatomic Pt-Ce induced interlayer spacing engineering for highly-efficient ammonia electrosynthesis. *Adv. Energy Mater.* **2023**, *13* (6), 2203201.

(14) Chen, F.-Y.; Elgazzar, A.; Pecaut, S.; Qiu, C.; Feng, Y.; Ashokkumar, S.; Yu, Z.; Sellers, C.; Hao, S.; Zhu, P.; et al. Electrochemical nitrate reduction to ammonia with cation shuttling in a solid electrolyte reactor. *Nat. Catal.* **2024**, *7* (9), 1032−1043.

(15) Murphy, E.; Liu, Y.; Matanovic, I.; Rüscher, M.; Huang, Y.; Ly, A.; Guo, S.; Zang, W.; Yan, X.; Martini, A. Elucidating electrochemical nitrate and nitrite reduction over atomically-dispersed transition metal sites. *Nat. Commun.* **2023**, *14* (1), 4554.
(16) Hao, D.; Chen, Z.-G.; Figiela, M.; Stepniak, I.; Wei, W.; Ni, B.-J. Emerging alternative for artificial ammonia synthesis through catalytic nitrate reduction. *J. Mater. Sci. Technol.* **2021**, *77* (30), 163−168.
(17) Liu, H.; Lang, X.; Zhu, C.; Timoshenko, J.; Rüscher, M.; Bai, L.; Guijarro, N.; Yin, H.; Peng, Y.; Li, J. Efficient electrochemical nitrate reduction to ammonia with copper-supported rhodium cluster and single-atom catalysts. *Angew. Chem., Int. Ed.* **2022**, *61* (23), No. e202202556.
(18) Fu, Y.; Wang, S.; Wang, Y.; Wei, P.; Shao, J.; Liu, T.; Wang, G.; Bao, X. Enhancing electrochemical nitrate reduction to ammonia over Cu nanosheets via facet tandem catalysis. *Angew. Chem., Int. Ed.* **2023**, *62* (26), No. e202303327.
(19) Das, S.; Laplaza, R.; Blaskovits, J. T.; Corminboeuf, C. Engineering frustrated Lewis pair active sites in porous organic scaffolds for catalytic CO_2 hydrogenation. *J. Am. Chem. Soc.* **2024**, *146* (23), 15806−15814.
(20) Yu, X. Y.; Huang, Z. Q.; Ban, T.; Xu, Y. H.; Liu, Z. W.; Chang, C. R. Finding natural, dense, and stable frustrated Lewis pairs on wurtzite crystal surfaces for small-molecule activation. *Angew. Chem., Int. Ed.* **2024**, *63* (23), No. e202405405.
(21) Xu, Z.-M.; Hu, Z.; Huang, Y.; Bao, S.-J.; Niu, Z.; Lang, J.-P.; Al-Enizi, A. M.; Nafady, A.; Ma, S. Introducing frustrated Lewis pairs to metal−organic framework for selective hydrogenation of N-heterocycles. *J. Am. Chem. Soc.* **2023**, *145* (27), 14994−15000.
(22) Li, W.; Gan, J.; Liu, Y.; Zou, Y.; Zhang, S.; Qu, Y. Platinum and frustrated Lewis pairs on ceria as dual-active sites for efficient reverse water-gas shift reaction at low temperatures. *Angew. Chem., Int. Ed.* **2023**, *135* (37), No. e202305661.
(23) Wang, Y.; Yang, R.; Ding, Y.; Zhang, B.; Li, H.; Bai, B.; Li, M.; Cui, Y.; Xiao, J.; Wu, Z.-S. Unraveling oxygen vacancy site mechanism of Rh-doped RuO_2 catalyst for long-lasting acidic water oxidation. *Nat. Commun.* **2023**, *14* (1), 1412.
(24) Jiang, S.; Zhang, R.; Liu, H.; Rao, Y.; Yu, Y.; Chen, S.; Yue, Q.; Zhang, Y.; Kang, Y. Promoting formation of oxygen vacancies in two-dimensional cobalt-doped ceria nanosheets for efficient hydrogen evolution. *J. Am. Chem. Soc.* **2020**, *142* (14), 6461−6466.
(25) Qin, Q.; Jang, H.; Jiang, X.; Wang, L.; Wang, X.; Kim, M. G.; Liu, S.; Liu, X.; Cho, J. Constructing Interfacial Oxygen Vacancy and Ruthenium Lewis Acid−Base Pairs to Boost the Alkaline Hydrogen Evolution Reaction Kinetics. *Angew. Chem., Int. Ed.* **2024**, *136* (3), No. e202317622.
(26) Fu, H.Q.; Zhou, M.; Liu, P.F.; Liu, P.; Yin, H.; Sun, K.Z.; Yang, H.G.; Al-Mamun, M.; Hu, P.; Wang, H.F.; Zhao, H. Hydrogen spillover-bridged Volmer/Tafel processes enabling ampere-level current density alkaline hydrogen evolution reaction under low overpotential. *J. Am. Chem. Soc.* **2022**, *144* (13), 6028−6039.
(27) Zhang, S.; Chen, D.; Guo, Y.; Zhang, R.; Zhao, Y.; Huang, Z.; Fan, J.; Ho, J. C.; Zhi, C. Piezoelectricity regulated ohmic contact in M/$BaTiO_3$ (M= Ru, Pd, Pt) for charge collision and hydrogen free radical production in ammonia electrosynthesis. *Mater. Today* **2023**, *66*, 17−25.
(28) Yao, J.; Lu, H.; Hou, B.; Xiao, Y.; Jia, L.; Li, D.; Wang, J. The promotional effect of La dopant on Co_3O_4 catalytic performance towards C_3H_8 combustion. *Catal. Lett.* **2021**, *151*, 1745−1754.
(29) Bae, J.; Shin, D.; Jeong, H.; Kim, B.-S.; Han, J. W.; Lee, H. Highly water-resistant La-doped Co_3O_4 catalyst for CO oxidation. *ACS Catal.* **2019**, *9* (11), 10093−10100.
(30) Wan, L.; Zhou, Q.; Wang, X.; Wood, T. E.; Wang, L.; Duchesne, P. N.; Guo, J.; Yan, X.; Xia, M.; Li, Y. F.; et al. Cu_2O nanocubes with mixed oxidation-state facets for (photo) catalytic hydrogenation of carbon dioxide. *Nat. Catal.* **2019**, *2* (10), 889−898.
(31) Chen, D.; Zhang, S.; Yin, D.; Quan, Q.; Zhang, Y.; Wang, W.; Meng, Y.; Liu, X.; Yip, S.; Yanagida, T. Controlled proton accessibility through carboxylic-based organic ligands for highly efficient and selective ammonia electrosynthesis. *Chem. Catal.* **2024**, *4* (7), 101024.
(32) Bae, S.-E.; Stewart, K. L.; Gewirth, A. A. Nitrate adsorption and reduction on Cu (100) in acidic solution. *J. Am. Chem. Soc.* **2007**, *129* (33), 10171−10180.
(33) Fang, J.-Y.; Zheng, Q.-Z.; Lou, Y.-Y.; Zhao, K.-M.; Hu, S.-N.; Li, G.; Akdim, O.; Huang, X.-Y.; Sun, S.-G. Ampere-level current density ammonia electrochemical synthesis using CuCo nanosheets simulating nitrite reductase bifunctional nature. *Nat. Commun.* **2022**, *13* (1), 7899.
(34) Guo, Y.; Zhang, R.; Zhang, S.; Hong, H.; Zhao, Y.; Huang, Z.; Han, C.; Li, H.; Zhi, C. Ultrahigh oxygen-doped carbon quantum dots for highly efficient H_2O_2 production via two-electron electrochemical oxygen reduction. *Energy Environ. Sci.* **2022**, *15* (10), 4167−4174.
(35) Wu, Y.; Liu, C.; Wang, C.; Lu, S.; Zhang, B. Selective transfer semihydrogenation of alkynes with H_2O (D_2O) as the H (D) source over a Pd-P cathode. *Angew. Chem., Int. Ed.* **2020**, *59* (47), 21170−21175.
(36) Liao, W.; Wang, J.; Ni, G.; Liu, K.; Liu, C.; Chen, S.; Wang, Q.; Chen, Y.; Luo, T.; Wang, X. Sustainable conversion of alkaline nitrate to ammonia at activities greater than 2 A cm^{-2}. *Nat. Commun.* **2024**, *15* (1), 1264.
(37) Zhang, S.; Hong, H.; Zhang, R.; Wei, Z.; Wang, Y.; Chen, D.; Li, C.; Li, P.; Cui, H.; Hou, Y.; et al. Modulating the leverage relationship in nitrogen fixation through hydrogen-bond-regulated proton transfer. *Angew. Chem., Int. Ed.* **2025**, *137* (1), No. e202412830.
(38) Wang, M.; Li, S.; Gu, Y.; Xu, W.; Wang, H.; Sun, J.; Chen, S.; Tie, Z.; Zuo, J.-L.; Ma, J. Polynuclear cobalt cluster-based coordination polymers for efficient nitrate-to-ammonia electroreduction. *J. Am. Chem. Soc.* **2024**, *146* (29), 20439−20448.
(39) Qi, D.; Lv, F.; Wei, T.; Jin, M.; Meng, G.; Zhang, S.; Liu, Q.; Liu, W.; Ma, D.; Hamdy, M. S. High-efficiency electrocatalytic NO reduction to NH_3 by nanoporous VN. *Nano Res. Energy* **2022**, *1* (2), No. e9120022.
(40) Xu, H.; Chen, J.; Zhang, Z.; Hung, C. T.; Yang, J.; Li, W. In situ confinement of ultrasmall metal nanoparticles in short mesochannels for durable electrocatalytic nitrate reduction with high efficiency and selectivity. *Adv. Mater.* **2023**, *35* (2), 2207522.
(41) Yu, W.; Yu, J.; Huang, M.; Wang, Y.; Wang, Y.; Li, J.; Liu, H.; Zhou, W. Laser-controlled tandem catalytic sites of CuNi alloys with ampere-level electrocatalytic nitrate-to-ammonia reduction activities for Zn−nitrate batteries. *Energy Environ. Sci.* **2023**, *16* (7), 2991−3001.
(42) Li, Y.; Lu, Z.; Zheng, L.; Yan, X.; Xie, J.; Yu, Z.; Zhang, S.; Jiang, F.; Chen, H. The synergistic catalysis effect on electrochemical nitrate reduction at the dual-function active sites of the heterostructure. *Energy Environ. Sci.* **2024**, *17* (13), 4582−4593.
(43) Zhang, R.; Hong, H.; Liu, X. H.; Zhang, S. C.; Li, C.; Cui, H. L.; Wang, Y. B.; Liu, J. H.; Hou, Y.; Li, P.; et al. Molecular engineering of a metal-organic polymer for enhanced electrochemical nitrate-to-ammonia conversion and zinc nitrate batteries. *Angew. Chem., Int. Ed.* **2023**, *62* (48), No. e202309930.

https://doi.org/10.1021/jacs.5c11084
J. Am. Chem. Soc. 2025, 147, 41433−41442